Available online at www.sciencedirect.com
ScienceDirect
International Journal of Heat and Mass Transfer 50 (2007) 367–380
International Journal of HEAT and MASS TRANSFER
www.elsevier.com/locate/ijhmt

Effects of Mach number and Reynolds number on jet array impingement heat transfer

Matt Goodro [a,b], Jongmyung Park [a,b], Phil Ligrani [a,b,d,*], Mike Fox [c,1], Hee-Koo Moon [c,1]

[a] Department of Mechanical Engineering, 50 S. Central Campus Drive, MEB 2110, University of Utah, Salt Lake City, UT 84112 9208, United States
[b] Convective Heat Transfer Laboratory, 50 S. Central Campus Drive, MEB 2110, University of Utah, Salt Lake City, UT 84112 9208, United States
[c] Aero/Thermal and Heat Transfer, Solar Turbines Inc., 2200 Pacific Highway, P.O. Box 85376, Mail Zone C-9, San Diego, CA 92186 5376, United States
[d] Turbomachinery Laboratory, Department of Engineering Science, Parks Road, Oxford University, Oxford OX1 3PJ, United Kingdom

Received 9 April 2006; received in revised form 10 June 2006
Available online 17 August 2006

Abstract

Experimental results from the present study show substantial, independent Mach number effects (as the Reynolds number is held constant) for an array of impinging jets. The present discharge coefficients, local and spatially averaged Nusselt numbers, and local and spatially averaged recovery factors are unique because (i) these data are obtained at constant Reynolds number as the Mach number is varied, and at constant Mach number as the Reynolds number is varied, and (ii) data are given for jet impingement Mach numbers up to 0.74, and for Reynolds numbers up to 60,000. As such, results are given for experimental conditions not previously examined, which are outside the range of applicability of existing correlations.

Keywords: Impingement cooling; Internal cooling; Gas turbines; Heat transfer augmentation

1. Introduction

Exposure to hot gasses or hot liquids generates undesirable heat in a wide range of applications. Impingement cooling is an attractive method for the removal of these heat loads because of its relativity high effectiveness. The main objective of impingement cooling is maximum heat removal with minimal coolant mass flow rates. To achieve this, jets of impinging fluid are frequently delivered by orifices integrated into internal structures within the component in need of heat removal. In the example of cooling leading edge regions of turbine blades and vanes, the impingement air enters the leading edge cavity from an adjacent cavity through a series of cross-over holes on the partition wall between the two cavities. The cross-over jets then impinge on the concave leading-edge wall and then exit either through film cooling holes, or though exit passages which lead to another part of the airfoil. Spanwise lines of impingement jets are produced with this arrangement which direct cooling air on high external heat load regions, such as the stagnation region [1]. Impingement cooling is also often used to cool parts of the combustor in gas turbine engines, including combustion chamber liners, transition pieces, and splash plates. In each case, impinging jets can be used individually or in arrays [2].

The effects of changing impingement plate geometric and configuration parameters, as well as physical parameters in flows with low Mach numbers, and relatively low speeds are considered in a variety of existing publications. The effects of Reynolds number and streamwise/spanwise hole spacing in low-speed impingement cooling are addressed by Kercher and Tabakoff [3] and Chance [4]. Metzger et al. [5] and Chupp et al. [6] address heat transfer with a semi-circular concave region with a line of circular jets impinging on the apex addressing the effects of target

* Corresponding author. Address: Turbomachinery Laboratory, Department of Engineering Science, Parks Road, Oxford University, Oxford OX1 3PJ, United Kingdom. Tels.: +44 1865 288734, +44 1865 288723; fax: +44 1865 288756.
E-mail address: phil.ligrani@eng.ox.ac.uk (P. Ligrani).
[1] Tel.: +1 619 544 5477; Pager: +1 619 526 4601.

0017-9310/$ - see front matter © 2006 Elsevier Ltd. All rights reserved.
doi:10.1016/j.ijheatmasstransfer.2006.06.007

Nomenclature

A	impingement hole area
A_{ht}	heat transfer area on the target plate
c_a	impingement air flow sonic velocity
c_i	impingement air flow ideal sonic velocity
C_D	discharge coefficient
D	diameter of an individual impingement hole
h_{loss}	heat transfer coefficient to account for convection and radiation loss from back side of target plate
k	ratio of specific heats
$\dot{m}$	impingement air mass flow rate
M_a	impingement air flow Mach number
M_i	impingement air flow ideal Mach number
Nu	local Nusselt number
Nu_c	corrected local Nusselt number
$\overline{Nu}$	line-averaged Nusselt number
$\overline{Nu}_c$	corrected line-averaged Nusselt number
$\overline{\overline{Nu}}$	spatially averaged Nusselt number
$\overline{\overline{Nu}}_F$	spatially averaged Nusselt number from Florschuetz et al. [9] correlation
P_a	impingement air static pressure
P_i	impingement air ideal static pressure
P_{0j}	impingement air stagnation pressure
Q	total power provided to the thermofoil heater
q_{rf}	radiation heat flux from front side (or impingement side) of the target plate
q_{rb}	radiation heat flux from back side of the target plate
q_{cf}	convection heat flux from front side (or impingement side) of the target plate
q_{cb}	convection heat flux from back side of the target plate
R	ideal gas constant
Re_j	impingement air flow Reynolds number
RF	recovery factor
$T_{ambient}$	ambient static temperature
T_b	local temperature on the back surface of the polystyrene target plate
T_W	local target surface temperature on the surface of the heater adjacent impingement air
T_{AW}	local adiabatic target surface temperature
T_i	impingement air ideal static temperature
T_j	impingement air static temperature
T_{0j}	impingement air stagnation temperature
T^*_{0j}	corrected impingement air stagnation temperature to give zero spatially averaged surface heat flux
T_{tc}	local thermocouple temperature between the heater and the polystyrene target plate
u_a	impingement air velocity
u_i	impingement air ideal velocity
x	streamwise coordinate
y	spanwise coordinate
z	normal coordinate
X	streamwise distance between centerlines of adjacent impingement holes
Y	spanwise distance between centerlines of adjacent impingement holes
Z	distance between target plate and impingement hole plate

Greek symbols

α	air thermal conductivity
ρ_a	impingement air static density
ρ_i	impingement air ideal static density
μ	absolute viscosity
σ	Boltzman constant
ε_f	emissivity of the front surface of the target plate
ε_{inf}	emissivity of a plate located opposite to the target plate

spacing, hole spacing, and jet Reynolds number. The influences of cross-flow on a single line of jets is examined by Metzger and Korstad [7], showing that target spacing, jet Reynolds number, and the relative strengths of the jet flow and the cross-flow influence heat transfer on the target wall. In another paper, Metzger et al. [8] present heat transfer characteristics measured on a target surface beneath a two-dimensional array of impinging jets also in low-speed flow that indicate in-line jet impingement hole patterns provide better heat transfer than staggered arrangements. Florschuetz et al. [9] includes data on channel cross-flow mass velocity and jet mass velocity (where ratios range from 0 to 0.8), in addition to a correlation with gives Nusselt number dependence on these parameters, as well as on jet impingement plate geometry, Prandtl number, and Reynolds number. Different cross-flow schemes on impingement heat transfer in low-speed flows are considered by Obot and Trabold [10] who arrive at the conclusion that for a given cross-flow scheme and constant jet diameter d, higher heat transfer coefficients are obtained as the number of jets over a fixed target area increases and that progressively lower performance is obtained as the cross-flow is restricted to exit through two opposite sides, and then, through one side of the passage between the impingement hole plate and the target plate. Bunker and Metzger [11] present detailed local heat transfer distributions due to line jet impingement for leading edge regions, both with and without film extraction effects. Fox et al. [12] examine the effects of unsteady vortical structures on the adiabatic wall temperature distribution produced by a single impinging jet. Bailey and Bunker [13] investigate impingement arrays with inline jets in a "square array", with different axial and lateral jet spacings and relatively low Mach numbers. Included are correlations developed from these data

which extend the range of applicability of the correlations presented by Florschuetz et al. [9]. Other recent studies considered the effects of jet impingement on a leading edge/concave wall with roughness [14], and the effects of jets with mist and steam on a concave target surface [15]. Parsons et al. [16,17], Parsons and Han [18], Epstein et al. [19], and Mattern and Hennecke [20] show that rotational effects are important for jets impinging on flat surfaces at relatively low Reynolds numbers. However, there is little or no information available at higher jet Reynolds numbers and jet rotation numbers on concave surfaces relevant to engine conditions. Thus, it is evident that, aside from a few investigations, most of the impingement data from the open literature are obtained on flat, smooth surfaces. Brevet et al. [21] employ flat plates to consider one row of impinging jets in a test section with low speed flow in which the spent air is again constrained to exit in one direction. Effects of impingement distance, Reynolds number, and spanwise hole spacing on Nusselt number distributions lead to recommendations for optimal Z/d values of 2–5, and optimal spanwise hole spacings of 4–5 hole diameters. Brevet et al. [22] describe recovery factors and Nusselt numbers measured on a flat target surface beneath a single, compressible impingement jet. These authors have the distinction of separating the effects of Mach number and Reynolds number. Data sets with different Mach numbers and constant Reynolds number are obtained using different impingement hole plates with different hole diameters. They conclude that, increasing the Mach number (as the Reynolds number is constant) improves impingement heat transfer significantly for jet Mach numbers greater than 0.2.

Other recent studies by Lee et al. [23], Garimella and Nenaydykh [24], and Shuja et al. [25] address the effects of nozzle geometry on heat transfer and fluid flow, whereas Siba et al. [26], Chung and Luo [27], and Abdon and Sundén [28] use experimental and numerical approaches to consider the influences of turbulent impingement jets. In another numerical investigation, Yong [29] investigates the hydrodynamic and heat transfer behavior of circular liquid jets. Laschefski et al. [30] also uses a numerical approach to investigate of heat transfer produced by rows of rectangular impinging jets. Seyedein et al. [31] report heat transfer characteristics from confined multiple turbulent impinging slot jets, and Rhee et al. [32] describe heat transfer, mass transfer, and flow characteristics from arrays of effusion holes.

Although the number of existing impingement cooling studies is considerable, new innovative cooling configurations are being used in gas turbines, which require additional investigation to account for a number of currently unexplored effects and their influence on impingement heat transfer. Two of the most important of these unexplored areas are the independent effects of Mach number and Reynolds number for an array of impinging jets. The present study provides data on these effects for an array of impinging jets in the form of discharge coefficients, local and spatially averaged Nusselt numbers, and local and spatially averaged recovery factors. The data are unique, not only because data are given for impingement jet Mach numbers as high as 0.74 and impingement jet Reynolds numbers as high as 60,000, but also because the effects of Reynolds number and Mach number are separated by providing data at constant Reynolds number as the Mach number is varied, and data at constant Mach number as the Reynolds number is varied. As such, the present impingement jet array study can considered a continuation of the investigation of Brevet et al. [22] wherein Mach number influences are investigated for a single impingement jet.

2. Experimental apparatus and procedures

2.1. Impingement flow facility, and impingement plate

Schematic diagrams of the facility used for heat transfer measurements are presented in Figs. 1 and 2. The facility is constructed of 6.1 mm thick ASTM A38 steel plates, and A53 Grade B ARW steel piping, and is open to the

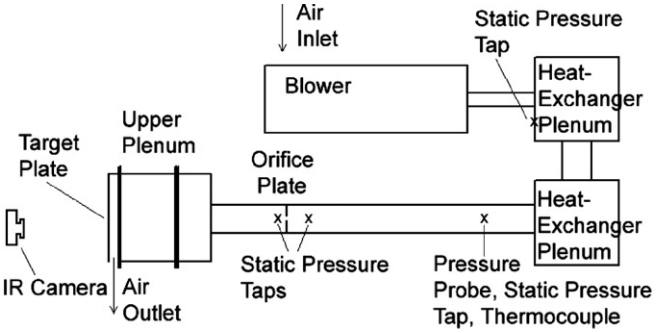

Fig. 1. Impingement flow facility.

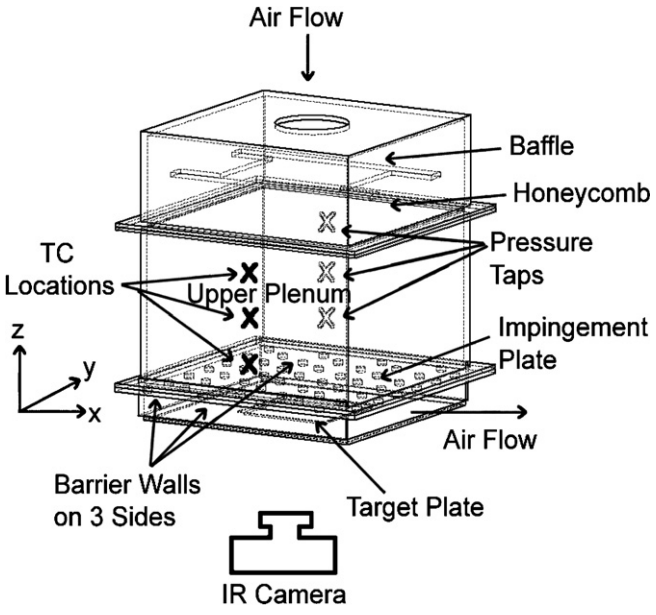

Fig. 2. Impingement flow facility test section, including impingement plenum, and impingement channel.

laboratory air at its inlet and exit. Depending upon the required flow conditions, one of two blowers is employed. For the lower Reynolds numbers investigated, a New York Blower Co. 7.5 HP, size 1808 pressure blower is employed. For higher Reynolds numbers, a DRUM Industries, 50 HP, D807 pressure blower is employed. In each case, the air mass flow rate provided to the test section is measured (downstream of whichever blower is employed) using an ASME standard orifice plate, flow-mounted calibrated copper–constantan thermocouples, and Validyne DP15 pressure transducers (with diaphragms rated at 13.8 or 34.5 kPa) connected to DP10D Carrier Demodulators. The blower exits into a series of two plenums arranged in series (the upstream plenum is 0.63 m to a side and the downstream plenum measures 0.63 m × 0.77 m × 0.77 m). A Bonneville cross-flow heat exchanger is located within the plenum which is farther downstream. As the air exits the heat exchanger, and the second plenum, the air passes into a 0.22 m outer diameter pipe, which contains the ASME Standard orifice plate employed to measure the air mass flow rate. This pipe then connects to the 0.635 m × 0.635 m side of a plenum. Upon entering this plenum, the air first encounters a flow baffle used to distribute the flow, a honeycomb, and other flow straightening devices. These are followed by the impingement plenum (or upper plenum, located below the honeycomb and flow straightening devices) whose top dimensions are 0.635 m and 0.635 m, and whose height is 0.40 m.

Individual plates with holes used to produce the impingement jets are located at the bottom of this plenum, as shown in Fig. 2. A list of the impingement test plate configurations employed is given in Table 1. The plenum is thus designed so that different impingement plates can be installed at this location using a 9.5 mm thick polyurethane gasket and 1/4 in SAE J429 Grade 5 bolts. Fig. 3 shows that each impingement plate is arranged with 10 rows of holes in the streamwise direction, arranged so that holes in adjacent rows are staggered with respect to each other. With this arrangement, either 9 or 10 holes are located in each streamwise row. The spacing between holes in the streamwise direction X is then $8D$, and the spanwise spacing between holes in a given streamwise row Y is also $8D$. The thickness of each impingement plate is $1D$. The spacing between the hole exit planes and the target plate is denoted Z and is equal to $3D$. Note that the coordinate

Table 1
Impingement test plate configurations

Hole diameter (mm)	Plate thickness (mm)	Hole spacing, X, Y (mm)	X/D, Y/D
3	3	24.0	8
3.5	3.5	28.0	8
4.5	4.5	36.0	8
8	8	64.0	8
15	15	120.0	8
20	20	160.0	8

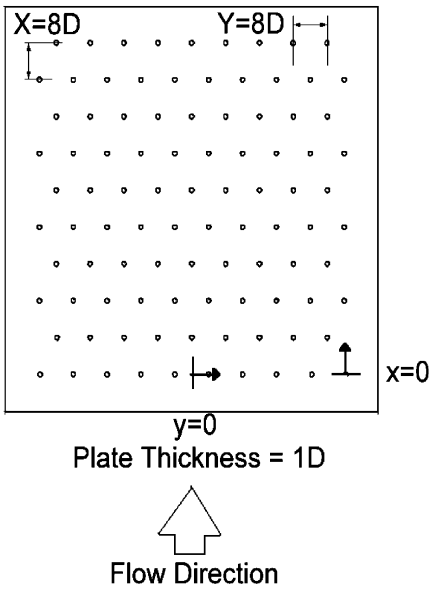

Fig. 3. Impingement test plate configuration.

system employed is also shown in Fig. 3. The impingement cooling flow which issues from these holes is contained within the channel formed by the impingement jet plate and the target surface, and is constrained to exit in a single direction, which here, is denoted as the x-direction. This channel is called the lower plenum. As different plates are employed with different sized impingement holes, this is accomplished using different polycarbonate spacers which are exactly $3D$ in height, and are sealed in place around three sides of the impingement channel. Plates with different impingement hole diameters are used to provide data at a variety of Mach numbers and Reynolds numbers. Specific hole sizes, mass flow rates, and pressure levels are employed so that data are obtained at different Mach numbers as the Reynolds number is constant, and at different Reynolds numbers as the Mach number is constant.

2.2. Target plate test surfaces for measurements of surface recovery factors and surface Nusselt numbers

Two different types of target plates are employed. Polycarbonate target plates are used for measurement of spatially resolved distributions of surface adiabatic surface temperature and surface recovery factor. Polycarbonate is chosen because of its strength, its low thermal conductivity (0.16 W/mK at 20 °C), and to minimize streamwise and spanwise conduction along the test surface, and thus, minimize "smearing" of spatially varying temperature gradients along the test surface. Each plate is 1.58 mm thick, and is mounted on the bottom surface of the plenum using grey cloth tape with PVC cement, a solvent containing methyl ethyl ketone, tetrahydrofuran, and acetone to seal the edges so that no leaks are present along the flow passage. A mounting frame is also employed to hold the target plate in place, to keep it smooth (without bending or wrin-

kles), and normal to the impingement jets, as testing is underway. Ten calibrated, copper–constantan thermocouples are placed at different streamwise and spanwise locations within the polycarbonate so that each senses a different temperature as data are acquired. Each one of these thermocouples is mounted approximately 0.02 cm just below the surface adjacent to the air containing the impingement fluid, to provide measurements of local surface temperatures, after correction for thermal contact resistance and temperature drop through the 0.16 cm thickness of polycarbonate. Thermocouple lead wires are placed in grooves along the polycarbonate, and bonded into place with epoxy, to minimize thermal disturbances resulting from their presence.

Spatially resolved distributions of surface heat transfer coefficients and Nusselt numbers are measured on polystyrene target plates with heaters and thermocouples attached. The custom-made HK5184R26 thermofoil heaters employed are manufactured by Minco Products Inc., and have a temperature rating of 100 °C. The etched-foil heating element within this device is encased between two layers of DuPont Kapton polyimide film, and is used to provide a constant surface heat flux boundary condition. This heater is located adjacent to the air stream with the impinging air jets. Its thermal conductivity is 0.2 W/mK at 20 °C. Polystyrene is chosen for the target plate because of its strength, and because it does not deform in shape at temperatures as high as 80 °C. It is also suitable because of its low thermal conductivity (0.09 W/mK at 20 °C), which results in minimal streamwise and spanwise conduction along the test surface. The back side of this polystyrene plate is viewed by the infrared camera as spatially resolved measurements of surface temperature are obtained. Each polystyrene target plate is 1.27 mm thick and each heater is approximately 0.3 mm thick, giving a total target plate thickness of 1.57 mm. Like the recovery factor target test plates, and these plates are mounted on the bottom surface of the plenum using grey cloth tape with PVC cement to seal the edges so that no leaks are present along the flow passage. A mounting frame is also again employed to hold the target plate in place, to keep it smooth (without bending or wrinkles), and normal to the impingement jets, as testing is underway. In order to detect different surface temperatures as testing is underway, nine calibrated, copper–constantan thermocouples are placed at different streamwise and spanwise locations within the polystyrene. Each one of these is mounted just below the surface adjacent to the air containing the impingement fluid, between the thermofoil heater and the polystyrene portion of the target plate. As each thermocouple is used to measure local surface temperature, corrections are made for thermal contact resistance and local temperature drop through the thermofoil heater. Thermocouple lead wires are placed in grooves in the polystyrene, and bonded into place with epoxy, to minimize thermal disturbances resulting from their presence. Because of the wear and degradation which results from exposure to different temperature levels as tests are conducted, these target plates are replaced with all new components after about 3 or 4 individual test sequences.

2.3. Local impingement air pressure and temperature measurements

As shown in Fig. 2, three wall pressure taps are located on the surface of the upper plenum, and eight wall pressure taps are located on the surface of the lower plenum for measurement of local static pressures. As tests are conducted, Validyne Model DP15-46 pressure transducers (with diaphragms rated at 13.8 or 34.5 kPa) driven by DP10D Carrier Demodulators are used to sense pressures from these static pressure tappings. Local airflow recovery temperatures are measured using two calibrated copper–constantan thermocouples located in the central part of the lower plenum, and three calibrated copper–constantan thermocouples located in the central part of the upper plenum. In each case, readings from either multiple thermocouples or multiple pressure taps are used to obtain average values of measured quantities for a given plenum. In some cases, additional surface pressure taps are located on exit side of the plate with the impingement holes. Voltages from the carrier demodulators and all thermocouples employed in the study are read sequentially using Hewlett-Packard HP44222T and HP44222A relay multiplexer card assemblies, installed in a Hewlett-Packard HP3497A low-speed data acquisition/control unit. This system provides thermocouple compensation electronically such that voltages for type T copper–constantan thermocouples are given relative to 0 °C. The voltage outputs from this unit are acquired by the Dell Precision 530 PC workstation through its USB port, using LABVIEW 7.0 software and a GPIB-USB-B adaptor made by National Instruments.

Because the overall volume and cross-sectional area of the upper plenum are large compared to the area of the impingement holes, the velocity of the air in this plenum is near zero. As a result, the static pressure measured at the wall static pressure taps is the same as the stagnation pressure, and is denoted P_{0j}, the impingement air stagnation pressure. The measured air recovery temperature in the upper plenum is then the same as the upper plenum static temperature and upper plenum stagnation temperature. This resulting value is denoted T_{0j}, the impingement stagnation temperature. After measurement of the impingement air mass flow rate at the pipe orifice plate, the impingement air mass flux is determined using $\rho_a u_a = \dot{m}/A$.

An iterative procedure is then used to determine the impingement static temperature T_j, and the impingement flow Mach number M_a. The first step in this procedure is estimation of the value of T_j. The local recovery temperature, which is measured in the lower plenum, is used for this estimation. The impingement static density, and

spatially averaged impingement jet velocity are then determined using $\rho_a = P_a/RT_j$, and $u_a = \dot{m}/\rho_a A$, respectively. Because the impingement flow vents to the laboratory, the local atmospheric pressure is used for P_a. Measurements of lower plenum static pressures using wall pressure taps confirm this approach. Next, the impingement air sonic velocity and Mach number are given by $c_a = (kRT_j)^{1/2}$ and $M_a = u_a/c_a$, respectively. Iterations using these analysis steps are then continued until the impingement static temperature and impingement Mach number are consistent with the isentropic equation given by

$$T_j = T_{0j}/[1 + M_a^2(k-1)/2] \tag{1}$$

With impingement static temperature T_j, impingement flow Mach number M_a, and other parameters known, the impingement Reynolds number is subsequently given by an equation of the form

$$Re_j = \rho_a u_a D/\mu \tag{2}$$

A Kiel-type stagnation pressure probe is used to measure the total pressure in the pipe at a position which is located upstream of the orifice plate employed to measure mass flow rate. A wall pressure tap located on the surface of the pipe, and a calibrated copper–constantan thermocouple positioned within the air stream are used to sense static pressure and flow recovery temperature, respectively, at the same streamwise location. Pressures and temperatures measured using the thermocouple, probe, and tap are sensed and processed using the same types of instrumentation mentioned earlier. The velocities deduced from this arrangement are used to provide a cross-check on the velocities deduced from mass flow rates, which are measured using the ASME standard orifice plate.

2.4. Discharge coefficient determination

The discharge coefficient is determined using

$$C_D = \rho_a u_a/\rho_i u_i \tag{3}$$

The first step in determining the ideal impingement mass flux $\rho_i u_i$ is obtaining an ideal impingement Mach number M_i using

$$P_{0j}/P_a = [1 + M_i^2(k-1)/2]^{k/k-1} \tag{4}$$

Next, impingement ideal static temperature T_i is determined using T_{0j}, the ideal Mach number M_i, and the appropriate ideal gas isentropic relationship. Impingement ideal static density is given by $\rho_i = P_a/RT_i$, and impingement ideal velocity is given by $u_i = M_i(kRT_i)^{1/2}$. Note that, in most cases, discharge coefficients are determined which are based on P_a, the spatially averaged static pressure at the exits of the impingement holes. In some other cases, local discharge coefficients for different impingement holes located along the length of the plate are determined, which are based on measurements of local static pressure measured at different surface pressure taps located along the exit side of the impingement plate.

2.5. Local recovery factor measurement

After the static temperature and stagnation temperatures of the impingement air are determined, the local surface recovery factor is determined at different target surface locations using

$$RF = (T_{AW} - T_j)/(T_{0j} - T_j) \tag{5}$$

Here, T_{AW} represents the local adiabatic surface temperature which is present with zero heat flux on the target surface. Note that some small variations of local adiabatic surface temperature T_{AW} and local recovery factor RF are present due to streamwise and spanwise conduction along the test surface, but these are minimized by the use of the polycarbonate target plate, and are included in the estimates of experimental uncertainty values for these two quantities. As tests are conducted and data are acquired, the impingement air jet stagnation temperature is maintained at or very near to the laboratory ambient temperature level $T_{0j} = T_{ambient}$. This is accomplished using liquid nitrogen in the Bonneville heat exchanger to cool the impingement air to the appropriate level as it passes through the facility. This thermal condition, $T_{0j} = T_{ambient}$, is then maintained for both the Nusselt number experiments and the recovery factor experiments to provide an appropriate basis of comparison between the data obtained from these two different types of experiments.

2.6. Local Nusselt number measurement

The power to the thermofoil heater, mounted on the target plate, is controlled and regulated using a variac power supply. Energy balances, and analysis to determine temperature values on the two surfaces of the target plate, then allow determination of the magnitude of the total convective power (due to impingement cooling) for a particular test. To determine the surface heat flux (used to calculate heat transfer coefficients and local Nusselt numbers), the total convective power level, provided by the particular thermofoil heater employed, is divided by the single surface area of this heater, denoted A_{ht}.

One step in this procedure utilizes a one-dimensional conduction analysis, which is applied between the surface *within* the target plate where the thermocouples are located (between the heater and the polystyrene target plate), and the ambient air environment behind the target plate. This is used to determine T_b, the local temperature on the back surface of the polystyrene target plate, adjacent to the surrounding ambient air environment. Also required for this analysis is T_{tc}, the local temperature within the target plate between the heater and the polystyrene plate, which is determined from thermocouple measurements. With these

temperatures known, the radiation heat flux and the convection heat flux from the back side of the target plate, q_{rb} and q_{cb}, respectively, are determined together using an equation of the form

$$q_{rb} + q_{cb} = h_{loss}(T_b - T_{ambient}) \quad (6)$$

where h_{loss} is assumed to be equal to 15 W/m^2 K [21]. The radiation heat flux q_{rf} on the front (or impingement side) of the target plate is determined using

$$q_{rf} = \sigma(1/\varepsilon_{inf} - 1/\varepsilon_f - 1)^{-1}(T_W^4 - T_{ambient}^4) \quad (7)$$

With this approach, the radiation heat flux is determined for an arrangement with multi-reflection between two infinite plates where each has a uniform temperature. ε_f and ε_{inf} are assumed to be equal to 0.9 for all conditions investigated. This approximate approach works well since $q_{rf}A_{ht}$ is generally only 3–6 percent of Q, the total amount of power provided to the thermofoil heater. Note that T_W, the local target surface temperature on the surface of the heater adjacent impingement air, must be known to determine q_{rf}. Because of the inter-dependence of T_W, q_{rf}, and q_{cf} (the convection heat flux from the front side or impingement side of the target plate), an iterative procedure is required to determine these quantities. The next part of this procedure uses a one-dimensional conduction model for the heater, which includes source generation of thermal energy, to provide a relation between T_W, T_{tc}, and q_{cf}. Also included in the analysis is thermal contact resistance between the internal thermocouples and the adjacent heater.

The convection heat flux from the front side (or impingement side) of the target plate is then given by

$$q_{cf} = Q/A_{ht} - q_{rf} - q_{rb} - q_{cb} \quad (8)$$

The local Nusselt number is then given as

$$Nu = q_{cf}D/((T_W - T_{0j})\alpha) \quad (9)$$

Modified local Nusselt numbers are also determined, which are based on the $(T_W - T^*_{0j})$ and the $(T_W - T_{AW})$ temperature differences. The determination of these parameters is discussed later in the paper.

Spatially resolved temperature distributions along the target test surface are determined using infrared imaging in conjunction with thermocouples, energy balances, digital image processing, and *in situ* calibration procedures. These are then used to determine spatially resolved surface Nusselt numbers. To accomplish this, the infrared radiation emitted by the heated interior surface of the channel is captured using a Thermacam PM390 Infrared Imaging Camera, which operates at infrared wavelengths from 3.4 μm to 5.0 μm. Temperatures, measured using the calibrated, copper–constantan thermocouples distributed along the test surface adjacent to the flow, are used to perform the *in situ* calibrations simultaneously as the radiation contours from surface temperature variations are recorded.

This is accomplished as the camera views the test surface from behind, as shown in Fig. 2. In general, six thermocouple junction locations are present in the infrared field viewed by the camera. The exact spatial locations and pixel locations of these thermocouple junctions and the coordinates of the field of view are known from calibration maps obtained prior to measurements. During this procedure, the camera is focused, and rigidly mounted and oriented relative to the test surface in the same way as when radiation contours are recorded. Voltages from the thermocouples are acquired using the apparatus mentioned earlier. With these data, gray scale values at pixel locations within video taped images from the infrared imaging camera are readily converted to local Nusselt number values. Because such calibration data depend strongly on camera adjustment, the same brightness, contrast, and aperture camera settings are used to obtain the experimental data. The *in situ* calibration approach rigorously and accurately accounts for these variations.

Images from the infrared camera are recorded as 8-bit gray scale directly into the memory of a Dell Dimension XPS T800r PC computer using a Scion Image Corporation Frame grabber video card, and Scion image v.1.9.2 software. One set of 15–20 frames is recorded at a rate of about one frame per second. All of the resulting images are then ensemble averaged to obtain the final gray scale data image. This final data set is then imported into Matlab version 6.1.0.450 (Release 12.1) software to convert each of 256 possible gray scale values to local Nusselt number at each pixel location using calibration data. Each individual image covers a 256 × 256 pixel area.

2.7. Experimental uncertainty estimates

Uncertainty estimates are based on 95% confidence levels and are determined using methods described by Kline and McClintock [33] and Moffat [34]. Uncertainty of temperatures measured with thermocouples is ±0.15 °C. Spatial and temperature resolutions achieved with infrared imaging are about 0.1–0.2 mm, and 0.4 °C, respectively. This magnitude of temperature resolution is due to uncertainty in determining the exact locations of thermocouples with respect to pixel values used for the *in situ* calibrations. Local Nusselt number uncertainty is then about ±4.8%. Uncertainty magnitudes of local recovery factors and adiabatic surface temperatures are approximately ±2.4%, and 0.5 °C, respectively. Note that uncertainties of local Nusselt numbers, adiabatic surface temperatures, and recovery factors all include the effects of very small amounts of streamwise and spanwise conduction along the test surfaces employed. Reynolds number uncertainty is about ±2.0% for an Re_j value of 20,000.

3. Experimental results and discussion

Table 2 gives a summary of the experimental conditions covered by the present investigation.

Table 2
Experimental conditions employed in the present investigation

Experiment number	Re_j	M_a	D (mm)
1	59,900	0.16	20
2	59,700	0.21	15
3	59,300	0.38	8
4	5200	0.092	3
5	6400	0.1	3.5
5.5	8200	0.1	4.5
14	58,600	0.63	4.5
15	56,300	0.74	3.5

3.1. Impingement hole discharge coefficients

Discharge coefficient data for the present experimental conditions, which represent average values for all of the impingement holes at a particular experimental condition, are presented in Fig. 4. Here, all discharge coefficients are based on P_a equal to the ambient pressure measured at the exit of the impingement flow facility. The data presented here are measured at different impingement Mach numbers and a constant Reynolds number Re_j of 60,000, and at different impingement Reynolds numbers and a constant Mach number M_a of 0.1. Discharge coefficient values range between 0.73 and 0.90 with a general trend of decreasing discharge coefficients with increasing Reynolds number (as the impingement Mach number is held constant).

3.2. Determination of spatially averaged adiabatic surface temperature T^*_{0j}

To determine an appropriate reference temperature for the determination of heat transfer coefficients and Nusselt numbers, the convective heat power from the impingement side of the target plate q_{cf} is determined as it varies with $(T_W - T_{0j})$. Data are obtained at three different temperature differences. The largest temperature difference employed is always less than 30 °C to avoid variations of measured Nusselt numbers with variable property effects. Such convective heat power data then vary linearly with $(T_W - T_{0j})$. Such linear data are extrapolated to the $q_{cf} = 0$ axis to determine $(T_W - T^*_{0j})$. Note that the convective power is the value for the entire target plate. Consequently, the magnitude of T^*_{0j} is spatially averaged over the target plate heat transfer area, and as such, is the spatially averaged adiabatic surface temperature for the entire heated portion of the target plate at a particular experimental condition. Consequently, all Nusselt number data are obtained at three different values of $(T_W - T_{0j})$ to provide a means to determine T^*_{0j} for each experimental condition. All Nusselt numbers are then determined using

$$Nu = q_{cf}D/(A_{ht}(T_W - T^*_{0j})\alpha) \tag{10}$$

3.3. Baseline Nusselt numbers

Baseline Nusselt numbers are measured to provide checks on measurement apparatus and procedures. The baseline test plate and flow conditions employed for this purpose match ones used by Florschuetz et al. [9] with $Re_j = 34{,}500$, M_a approximately equal to 0, and an array of jets with $X = 5D$, $Y = 4D$, and $Z = 3D$. Like the investigation of Florschuetz et al. [9], the passage between the impingement plate and the target plate in the present arrangement is closed on three sides so that the effects of spent air cross-flow are considered. Fig. 5 shows a comparison of the results from the two investigations. The good agreement of the area-averaged data from the two sources validates the experimental procedures and apparatus employed in the present study. The present data are area-averaged over y/D from −8.0 to +8.0, and over $5D$ length segments in the streamwise direction. Also presented in this figure are local Nu data from the present investigation as they vary with x/D for $y/D = 4$ and $y/D = 8$, and $\overline{Nu}$ data which are line-averaged over y/D from −8.0 to +8.0.

The effect of the unheated starting length located upstream of the heated target plate is also investigated. This is done by adding an additional heater upstream of

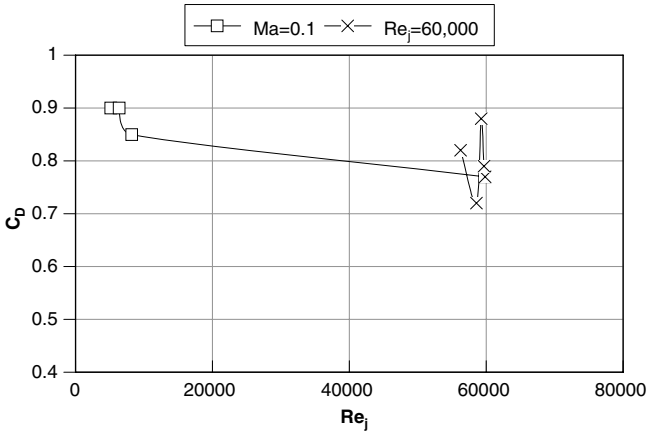

Fig. 4. Discharge coefficient data for $Re_j = 60{,}000$ and different Mach numbers, and for $M_a = 0.1$ and different impingement Reynolds numbers.

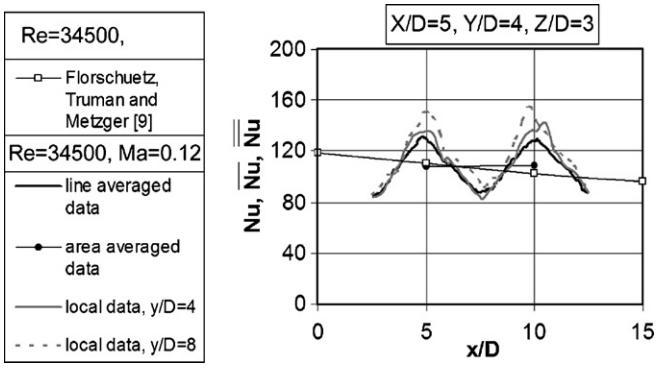

Fig. 5. Comparison of baseline Nusselt number data with correlation of Florschuetz et al. [9] for $Re_j = 34{,}500$, M_a approximately equal to 0, and an array of jets with $X = 5D$, $Y = 4D$, and $Z = 3D$.

the heater used on the target plate. Local and spatially averaged Nusselt numbers are then measured on the target plate, both with and without upstream heating, for $Re_j = 34{,}500$ and $M_a = 0.12$ with the same impingement hole plate as used for the other baseline data checks. The variation of local and spatially averaged Nusselt numbers between the two tests is only about 2%, at most, indicating minimal effect of thermal entry length on impingement heat transfer (for these particular experimental conditions).

3.4. Nusselt number variations with Reynolds number

Surface Nusselt number distributions are presented in Fig. 6 for $M_a = 0.10$, and Re_j values of 5200, 6400, and 8200. The different views of the test surface in the different parts of this figure are due to different infrared camera views of the target plate as impingement plates with different sized holes are employed on the opposite side. Note that, regardless of the Reynolds number, the qualitative distributions of local Nusselt number produced by each impingement jet are similar, with good periodic repeatability in the spanwise direction for each streamwise row of impact locations. This spanwise periodicity is also illustrated by the local Nu data presented in Fig. 7a for $x/D = 32$, and the same Re_j values.

Fig. 6 also shows that only one local maximum value is present in the Nu distribution underneath each jet. In general, magnitudes of these local jet maxima underneath the different impingement jets decrease as the flow develops in the streamwise direction and x/D increases, for particular M_a and Re_j values. This trend is also illustrated by local Nusselt number data presented as they vary with x/D in Fig. 7b for $y/D = 8$. Here, the smaller peak values near $x/D = 32$ and $x/D = 48$, which are positioned between the larger peak values, are due to local Nusselt number increases at spanwise locations approximately halfway between the impact points of nearby impinging jets. Another important conclusion apparent from Figs. 6, 7a and b is that local maximum Nu values generally increase at each x/D and y/D surface location as the Reynolds number increases.

Fig. 8 presents Nusselt numbers as they vary with x/D for the same experimental conditions, which are line-averaged over y/D from -8.0 to $+8.0$. Here, local maximum values are apparent, which are spaced approximately $8D$ apart, and are due to the impact of impingement jets from each different streamwise row of holes. Here, line-averaged

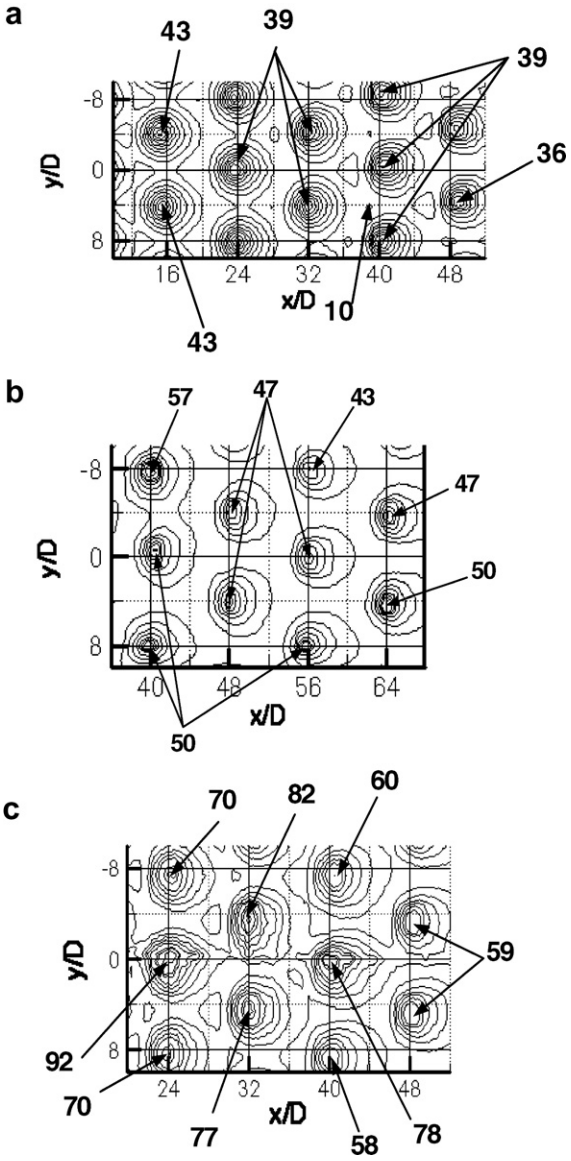

Fig. 6. Spatially resolved distributions of surface Nusselt number for $M_a = 0.10$, and Re_j values of (a) 5200, (b) 6400, and (c) 8200.

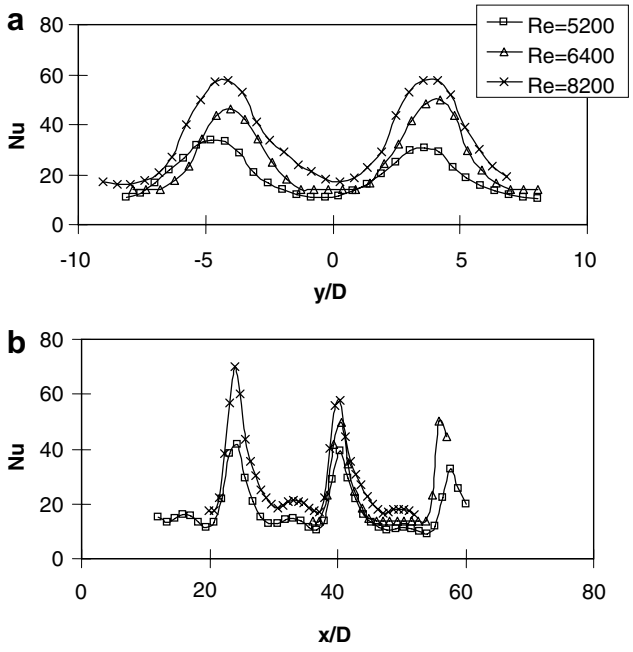

Fig. 7. Local surface Nusselt number variations for $M_a = 0.10$, and Re_j values of 5200, 6400, and 8200. (a) Variations with y/D for $x/D = 32$. (b) Variations with x/D for $y/D = 8$.

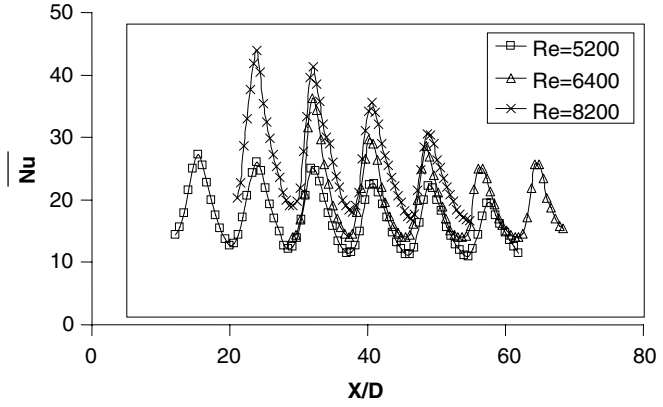

Fig. 8. Surface Nusselt number variations with x/D, which are line-averaged over y/D from −8.0 to +8.0, for $M_a = 0.10$, and Re_j values of 5200, 6400, and 8200.

$\overline{Nu}$ data generally increase with Re_j at each x/D location (provided M_a is constant at 0.1). Local peak line-averaged Nusselt numbers then consistently decrease at successive x/D locations for particular values of Re_j and M_a (which is consistent with the data presented in the previous two figures).

3.5. Nusselt number variations with Mach number

Local spatially resolved surface Nusselt number distributions for $Re_j = 60{,}000$ and M_a values from 0.16 to 0.74 are given in Fig. 9. Like the results in Fig. 6, the different views of the test surface shown by the data in the different parts of Fig. 9 are due to different infrared camera views of the target plate as impingement plates with different sized holes are employed on the opposite side. The local Nusselt number distributions which are produced by each impingement jet are qualitatively similar to each other and to the distributions shown in Fig. 6. This includes local distributions associated with each impingement impact area at different spanwise locations in each streamwise row.

This spanwise periodicity as y/D varies is also shown by the local Nusselt number data which are presented in Fig. 10b. These data are given for the same impingement Mach numbers at several different x/D values. Streamwise variations of local Nusselt numbers are then given in Fig. 10a for $y/D = 0$. For each x/D and y/D location, local Nusselt numbers are either invariant as the impingement Mach number increases, or increase with impingement Mach number. The smaller peak values present in each distribution in Fig. 10a near $x/D = 16$, $x/D = 32$, and $x/D = 48$, and $x/D = 64$ (which are positioned between the larger peak values) are due to local Nusselt number increases at spanwise locations approximately halfway between target surface impact regions of nearby impinging jets.

Corresponding line-averaged Nusselt number data as they vary with x/D are given in Fig. 11, also for

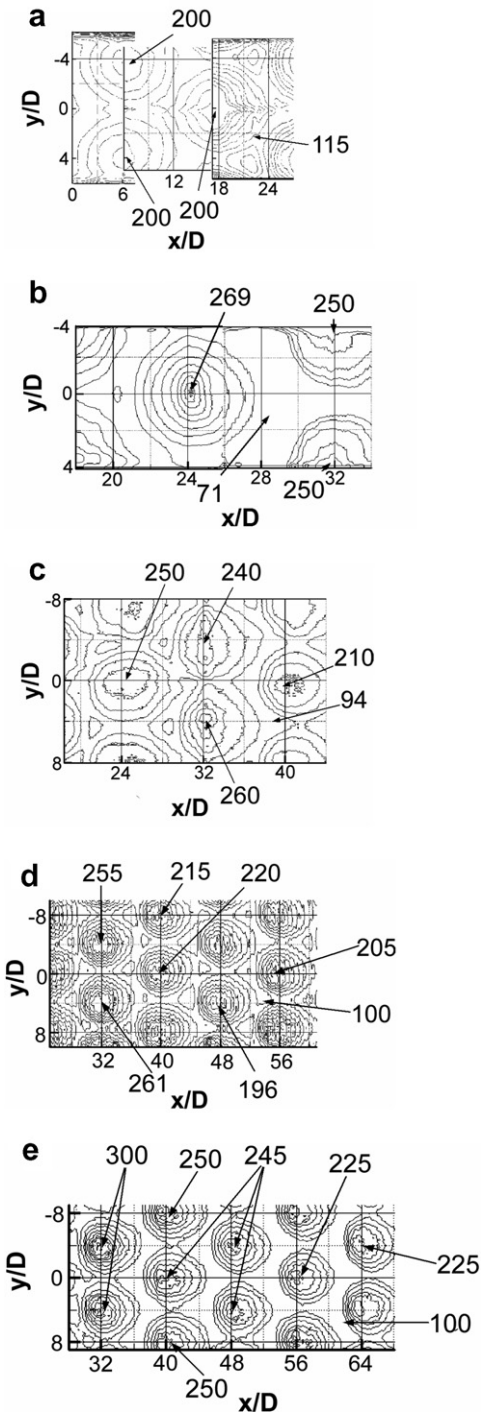

Fig. 9. Spatially resolved distributions of surface Nusselt number for $Re_j = 60{,}000$ and M_a values of (a) 0.16, (b) 0.21, (c) 0.38, (d) 0.63 and (e) 0.74.

$Re_j = 60{,}000$ and $M_a = 0.16$, 0.21, 0.38, 0.63, and 0.74. Like the data presented in Fig. 8, these data are also obtained by line-averaging over y/D values from −8.0 to +8.0. Fig. 11 shows that local maximum $\overline{Nu}$ values have the same approximate streamwise spacing as the streamwise spacing of the holes located on the impingement jet plate. Associated local maximum values here generally decrease at successive x/D locations for each value of

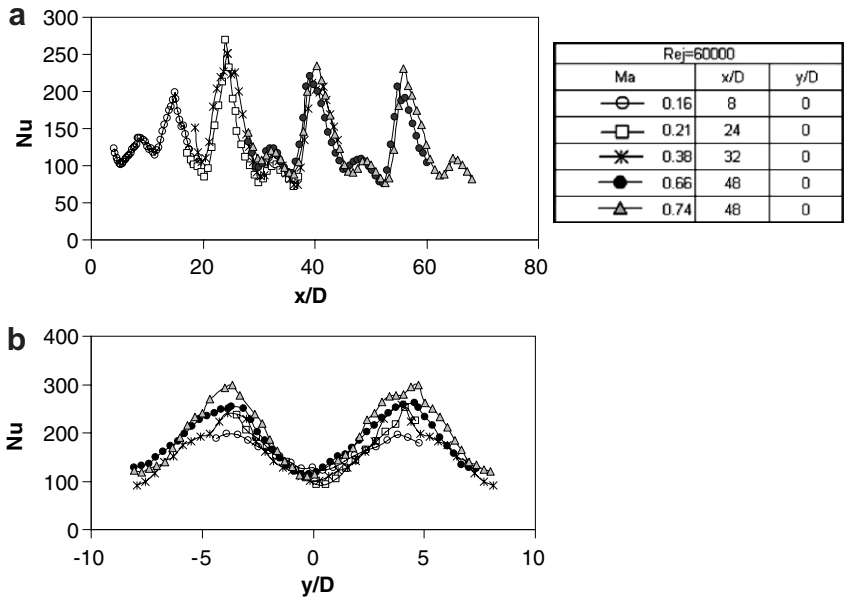

Fig. 10. Local surface Nusselt number variations for $Re_j = 60{,}000$ and M_a values of 0.16, 0.21, 0.38, 0.63, and 0.74. (a) Variations with x/D for $y/D = 0$. (b) Variations with y/D for $x/D = 8$, 32, 32, 32, and 32.

impingement Mach number, M_a. In most cases, line-averaged $\overline{Nu}$ values increase at each x/D location as M_a increases. Exceptions to this trend are exhibited by the $M_a = 0.21$ data which show higher peak values (compared to data measured at lower Mach numbers) near the $x/D = 16$, $x/D = 24$, and $x/D = 32$ locations.

3.6. Comparisons of spatially averaged Nusselt numbers with existing correlations, and development of a new correlation

Spatially averaged Nusselt numbers are compared to the correlation of Florschuetz et al. [9] in Fig. 12a and b. Each data point in these figures from the present investigation is determined by averaging local Nusselt number data over y/D values from -8.0 to $+8.0$, and over an x/D range of 8.0 (or $x/D = -4.0$ to $x/D = +4.0$) relative to the centers of the nominal jet impact locations (which correspond to the x/D centers of the impingement plate holes). The first of these figures shows $M_a = 0.10$ data for Re_j values of 5200, 6400, and 8200. Here, data from the present study show reasonably good matches to the correlation values from Florschuetz et al. [9] for all of these experimental conditions. Fig. 12b presents the present spatially averaged data for $Re_j = 60{,}000$, and M_a values of 0.16, 0.21, 0.38, 0.63, and 0.74. In this figure, the experimental data associated with $M_a = 0.16$ and $M_a = 0.21$ are in good agreement with the Florschuetz et al. [9] correlation. The present data then deviate from this correlation by larger amounts as the impingement Mach number increases further, with the largest deviation evident for $M_a = 0.74$. In general, the trends shown by the data in Fig. 12b are qualitatively consistent with results from Brevet et al. [22] for a single impingement jet.

The variation of spatially averaged Nusselt numbers with Mach number is shown in Fig. 12c. These data are given for specific x/D values, and for specific values of

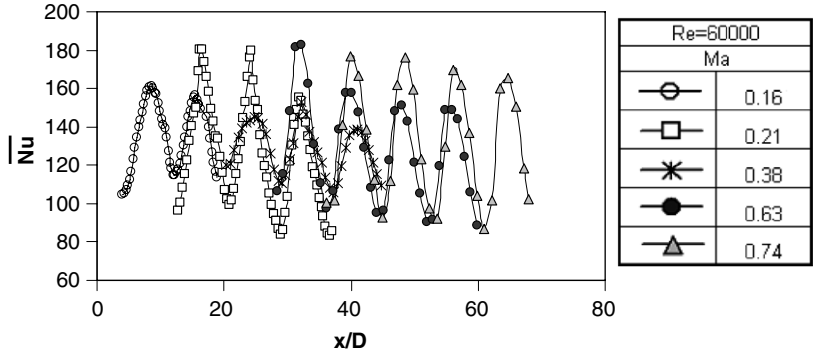

Fig. 11. Surface Nusselt number variations with x/D, which are line-averaged over y/D from -8.0 to $+8.0$, for $Re_j = 60{,}000$ and M_a values of 0.16, 0.21, 0.38, 0.63, and 0.74.

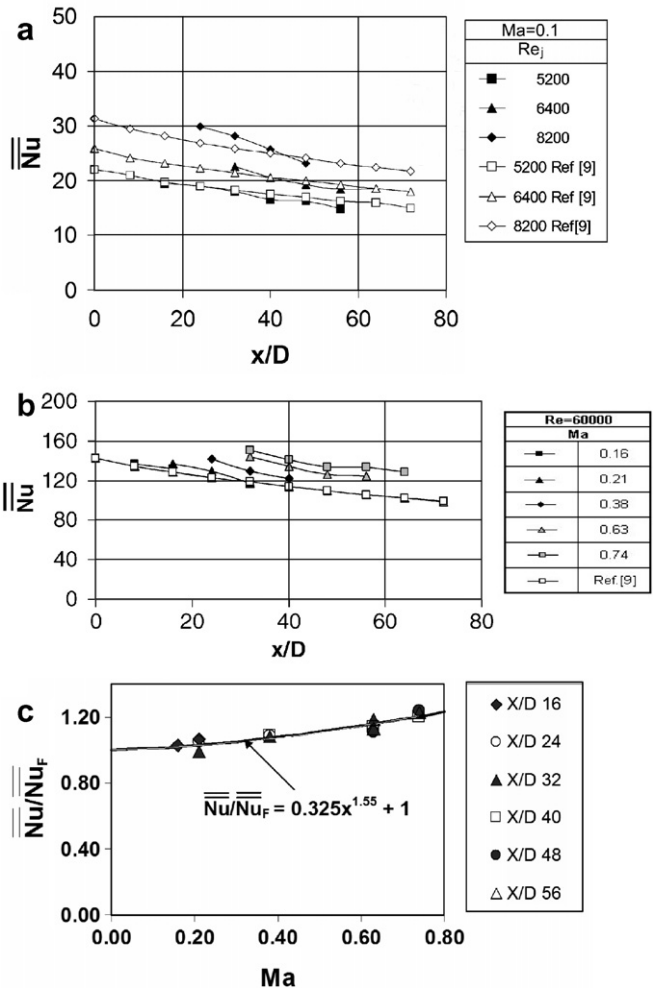

Fig. 12. Comparison of spatially averaged Nusselt numbers with correlation of Florschuetz et al. [9]. (a) Data for $M_a = 0.10$, and Re_j values of 5200, 6400, and 8200. (b) Data for $Re_j = 60{,}000$ and M_a values of 0.16, 0.21, 0.38, 0.63, and 0.74. (c) Nusselt number data at specific x/d locations correlated with respect to Mach number.

the impingement Mach number. The correlation equation which best represents these data is given by

$$\overline{\overline{Nu}}/\overline{\overline{Nu}}_F = 1.0 + 0.325M_a^{1.55} \quad (11)$$

As such, this correlation equation is valid for $Re_j = 60{,}000$, $0.21 \leqslant M_a \leqslant 0.74$, $X/D = 8$, $Y/D = 8$, $Z/D = 3$, and $20 \leqslant x/D \leqslant 60$.

3.7. Recovery factor data

Recovery factor data provide information on the variation of adiabatic surface temperature over the test surface. Examples are shown in Fig. 13a–c for $Re_j = 60{,}000$ and $M_a = 0.74$. The contour plot data in Fig. 13a show higher values of recovery factor RF beneath and in the vicinity of impact locations of the impingement jets. This is because $T_{0j} = 23.27$ °C, which is approximately equal to T_{ambient} for these tests which gives T_j equal to −6.16 °C. As a result, there is heat transfer to the impinging air streams from the surrounding air, an effect which is enhanced by the families of vortices associated with the jet, and the enhanced mixing and entrainment they produce of surrounding fluid to the jets [12]. Nearby jet impact locations, values of RF continue to be relatively high and in general, greater than 1.0, especially on the spanwise sides of impact locations. However, values are occasionally less than one at upstream and downstream locations. Such local variations and the quantitative variations associated with them are further illustrated by the local RF data presented as it varies with x/D for $y/D = 0$, 4, and 8 in Fig. 13b, and as RF varies with y/D for $x/D = 32$, 48, and 56 in Fig. 13c. Note that values of T_{AW}, determined from RF data and spatially averaged over the test surface, approximately match magnitudes of T^*_{0j} for most all experimental conditions where these data are measured.

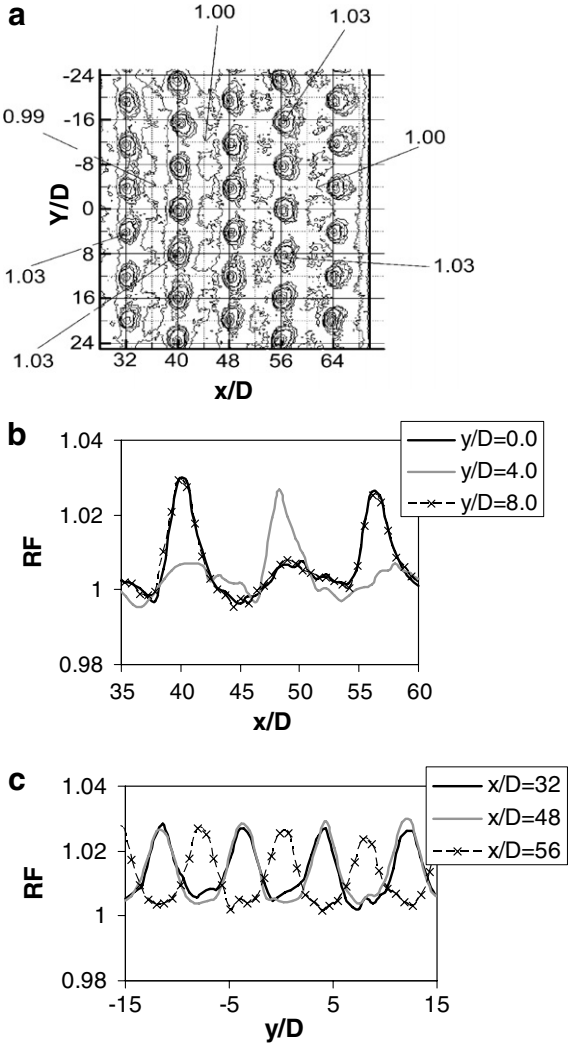

Fig. 13. Recovery factor data for $Re_j = 60{,}000$ and $M_a = 0.74$. (a) Local surface recovery factor distribution. (b) Local surface recovery factor data as it varies with x/D for $y/D = 0$, 4, and 8. (c) Local surface recovery factor data as it varies with y/D for $x/D = 32$, 48, and 56.

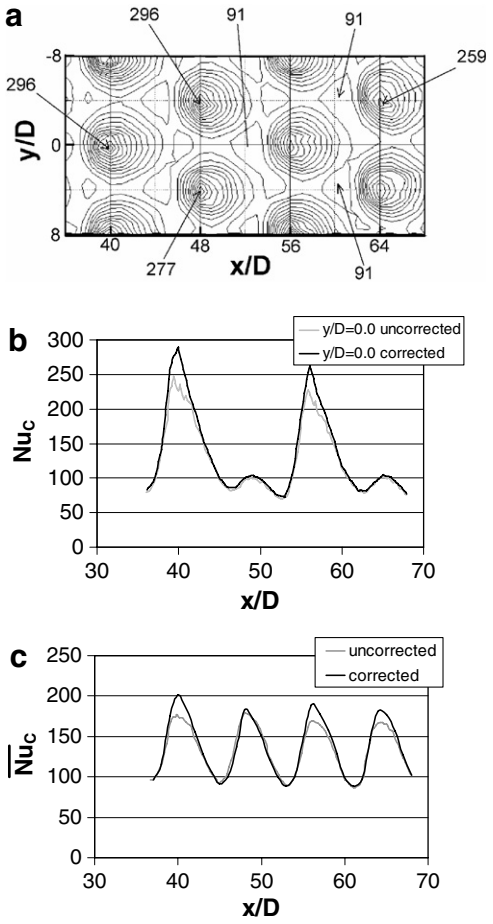

Fig. 14. Corrected and uncorrected surface Nusselt number data for $Re_j = 60{,}000$ and $M_a = 0.74$. (a) Local corrected surface Nusselt number distribution. (b) Local surface Nusselt number data as it varies with x/D for $y/D = 0$. (c) Surface Nusselt number variations with x/D which are line-averaged over y/D from -8.0 to $+8.0$.

3.8. Nusselt number data corrected using local recovery factors

The local and line-averaged Nusselt number data presented in Fig. 14a–c are based on the difference between the local, spatially varying measured surface temperature T_W, and the local adiabatic surface temperature T_{AW}, determined from recovery factor data given in Fig. 13a. This is accomplished by correcting local Nusselt number values using the equation given by

$$Nu_c = Nu(T_W - T^*_{0j})/(T_W - T_{AW}) \quad (12)$$

Recall that T^*_{0j} represents the adiabatic surface temperature, spatially averaged over the test plate. The results in Fig. 14a–c are given for $Re_j = 60{,}000$ and $M_a = 0.74$. A comparison of Fig. 14a with results presented in Fig. 9d then shows that local corrected Nusselt numbers Nu_c based on local $(T_W - T_{AW})$ (i.e. Fig. 14a) have slightly higher peaks than local Nu values based on $(T_W - T^*_{0j})$ (Fig. 9d). This trend is also illustrated by the local Nusselt number data presented as it varies with x/D (for $y/D = 0$) in Fig. 14b, as well as by the line-averaged Nusselt number data given in Fig. 14c. The relative differences between corrected and uncorrected data in these figures are generally quite small because recovery factors in Fig. 13a–c are close to 1.00 with the largest values in the vicinity of 1.03. As a result, spatially averaged Nusselt numbers are approximately the same regardless of whether they are based upon $(T_W - T_{AW})$ or $(T_W - T^*_{0j})$.

4. Summary and conclusions

In the present investigation, data are given for an array of impinging jets in the form of discharge coefficients, local and spatially averaged Nusselt numbers, and local and spatially averaged recovery factors. The spacing between holes in the streamwise direction X is then $8D$, and the spanwise spacing between holes in a given streamwise row Y is also $8D$. The thickness of each impingement plate is $1D$, and the spacing between the hole exit planes and the target plate is denoted Z and is equal to $3D$.

Experimental spatially averaged, surface Nusselt number data obtained for a constant impingement Mach number M_a of 0.1, and different Reynolds numbers Re_j from 5200 to 8200 show good agreement with the correlation of Florschuetz et al. [9]. Nusselt number data obtained at a constant Reynolds number of 60,000 and different impingement Mach numbers also shows good agreement with the Florschuetz et al. [9] correlation, provided $M_a = 0.16$ and $M_a = 0.21$. Measured spatially averaged results for $Re_j = 60{,}000$ then deviate from this correlation by larger amounts as the impingement Mach number increases further, with the largest deviation evident for $M_a = 0.74$. A new correlation equation for spatially averaged Nusselt numbers is then presented for this range of Mach numbers. The variations represented by this correlation are due to local Nusselt numbers and line-averaged Nusselt numbers, which generally increase with Mach number at different x/D and y/D locations, provided $Re_j = 60{,}000$ and impingement Mach number M_a is greater than 0.21. Local, spatially resolved Nusselt number data also show that only one local maximum value is present underneath each jet, with local peak line-averaged $\overline{Nu}$ values, which generally decrease with streamwise development at successive x/D locations.

Local spatially resolved Nusselt number data obtained a Mach number M_a of 0.74, and $Re_j = 60{,}000$ are also corrected to account for local variations of the adiabatic surface temperature, which are determined from local recovery factor data. Local corrected Nusselt numbers Nu_c based on local $(T_W - T_{AW})$ then have higher peaks than local Nu values based on $(T_W - T^*_{0j})$. This is because local recovery factor RF data are higher beneath and in the vicinity of impact locations of the impingement jets, with values as large as 1.03.

Acknowledgments

The present investigation is supported by Solar Turbines Inc of San Diego, California, USA.

References

[1] H. Martin, Heat and mass transfer between impinging gas jets and solid surfaces, Adv. Heat Transfer 13 (1977) 1–60.
[2] A. Schulz, Combuster liner cooling technology in scope of reduced pollutant formation and rising thermal efficiencies, Heat Transfer Gas Turbine Syst., Ann. New York Acad. Sci. 934 (2001) 135–146.
[3] D.M. Kercher, W. Tabakoff, Heat transfer by a square array of round air jets impinging perpendicular to a flat surface including the effect of spent air, ASME Trans. J. Eng. Power 92 (1970) 73–82.
[4] J.L. Chance, Experimental investigation of air impingement heat transfer under an array of round jets, TAPPI 57 (6) (1974) 108–112.
[5] D.E. Metzger, T. Yamashita, C. Jenkins, Impingement cooling of concave surfaces with lines of circular air jets, ASME Trans. J. Eng. Power 91 (1971) 149–158.
[6] R. Chupp, H. Helms, P. McFadden, T. Brown, Evaluation of internal heat-transfer coefficients for impingement cooled turbine airfoils, AIAA J. Aircraft 6 (3) (1969) 203–208.
[7] D.E. Metzger, R. Korstad, Effects of crossflow on impingement heat transfer, ASME Trans. J. Eng. Power 94 (1972) 35–41.
[8] D.E. Metzger, L.W. Florschuetz, D.I. Takeuchi, R.D. Behee, R.A. Berry, Heat transfer characteristics for inline and staggered arrays of circular jets with crossflow of spent air, ASME Trans. J. Heat Transfer 101 (1979) 526–531.
[9] L.W. Florschuetz, C.R. Truman, D.E. Metzger, Streamwise flow and heat transfer distributions for jet array impingement with crossflow, ASME Trans. J. Heat Transfer 103 (1981) 337–342.
[10] N.T. Obot, T.A. Trabold, Impingement heat transfer within arrays of circular jets: Part 1—Effects of minimum, intermediate, and complete crossflow for small and large spacings, ASME Trans. J. Heat Transfer 109 (1987) 872–879.
[11] R. Bunker, D.E. Metzger, Local heat transfer in internally cooled turbine airfoil leading edge regions: Part 1—Impingement cooling without film extraction, ASME Trans. J. Turbomach. 112 (1990) 451–458.
[12] M.D. Fox, M. Kurosaka, L. Hedges, K. Hirano, The influence of vortical structures on the thermal fields of jets, J. Fluid Mech. 255 (1993) 447–472.
[13] J.C. Bailey, R.S. Bunker, Local heat transfer and flow distributions for impinging jet arrays of dense and sparse extent, ASME paper no. GT-2002-30473, 2002.
[14] M.E. Taslim, Y. Pan, K. Bakhtari, Experimental racetrack shaped jet impingement on a roughened leading-edge wall with film holes, ASME paper no. GT-2002-30477, 2002.
[15] X. Li, J.L. Gaddis, T. Wang, Mist/stream heat transfer with jet impingement onto a concave surface, ASME paper no. GT-2002-30475, 2002.
[16] J.A. Parsons, J.C. Han, C.P. Lee, Rotation effect on jet-impingement heat transfer in smooth rectangular channels with four heated walls and radial crossflow, ASME Trans. J. Turbomach. 120 (1996) 79–85.
[17] J.A. Parsons, J.C. Han, C.P. Lee, Rotation effect on jet-impingement heat transfer in smooth rectangular channels with four heated walls and coolant extraction, ASME paper no. GT-2003-38905, 2003.
[18] J.A. Parsons, J.C. Han, Rotation effect on jet impingement heat transfer in smooth rectangular channels with coolant extraction, Int. J. Rotating Mach. 7 (2001) 87–103.
[19] A.H. Epstein, J.L. Kerrebrock, J.J. Koo, U.Z. Preiser, Rotational effects on impingement cooling, in: Symposium on Transport Phenomena in Rotating Machinery, Honolulu, 1985.
[20] C. Mattern, D.K. Hennecke, Influence of rotation on impingement cooling, ASME paper no. GT-1996-161, 1996.
[21] P. Brevet, C. Dejeu, E. Dorignac, M. Jolly, J.J. Vullierme, Heat transfer to a row of impinging jets in consideration of optimization, Int. J. Heat Mass Transfer 45 (2002) 4191–4200.
[22] P. Brevet, E. Dorignac, J.J. Vullierme, Mach number effect on jet impingement heat transfer, Heat Transfer Gas Turbine Syst., Ann. New York Acad. Sci. 934 (2001) 409–416.
[23] D.H. Lee, J. Song, M.C. Jo, The effects of nozzle diameter on impinging jet heat transfer and fluid flow, J. Heat Transfer 126 (4) (2004) 554–557.
[24] S.V. Garimella, B. Nenaydykh, Nozzle-geometry effects in liquid jet impingement heat transfer, Int. J. Heat Mass Transfer 39 (14) (1996) 2915–2923.
[25] S.Z. Shuja, B.S. Yilbas, M.O. Budair, Influence of conical and annular nozzle geometric configurations on flow and heat transfer characteristics due to flow impingement onto a flat plate, Numer. Heat Transfer A 48 (9) (2005) 917–939.
[26] E.A. Siba, M. Ganesa-Pillai, K.T. Harris, A. Haji-Sheikh, Heat transfer in a high turbulence air jet impinging over a flat circular disk, J. Heat Transfer 125 (2) (2003) 257–265.
[27] Y.M. Chung, K.H. Luo, Unsteady heat transfer analysis of an impinging jet, J. Heat Transfer 124 (6) (2002) 1039–1048.
[28] A. Abdon, B. Sundén, Numerical investigation of impingement heat transfer using linear and non-linear two-equation turbulence models, Numer. Heat Transfer A 40 (6) (2001) 563–578.
[29] A.Y. Tong, A numerical study on the hydrodynamics and heat transfer of a circular liquid jet impinging onto a substrate, Numer. Heat Transfer A 44 (1) (2003) 1–19.
[30] H. Laschefski, T. Cziesla, G. Biswas, N.K. Mitra, Numerical investigation of heat transfer by rows of rectangular impinging jets, Numer. Heat Transfer A 30 (1) (1996) 87–101.
[31] S.H. Seyedein, M. Hasan, A.S. Mujumdar, Turbulent flow and heat transfer from confined multiple impinging slot jets, Numer. Heat Transfer A 27 (1) (1995) 35–51.
[32] D.H. Rhee, P.H. Yoon, H.H. Cho, Local heat/mass transfer and flow characteristics of array impinging jets with effusion holes ejecting spent air, Int. J. Heat Mass Transfer 46 (6) (2003) 1049–1061.
[33] S.J. Kline, F.A. McClintock, Describing uncertainties in single sample experiments, Mech. Eng. 75 (1953) 3–8.
[34] R.J. Moffat, Describing the uncertainties in experimental results, Exp. Therm. Fluid Sci. 1 (1) (1988) 3–17.